

Supporting Information

Giant in-plane vibrational and transport anisotropy in van der Waals Ta₂Ni₃Te₅

Haige Tan^{1#}, Ying Zhang^{1#}, Zhisheng Zhao^{2#}, Changlong Wang¹, Ranran Zhang³, Shasha Wang¹, Xiang Ma¹, Yan Feng¹, Meng Gu⁴, Yalin Lu¹, Juan Jiang^{2*}, Shunhong Zhang^{5*}, Bin Xiang^{1*}

¹Department of Materials Science & Engineering, CAS Key Lab of Materials for Energy Conversion, Anhui Laboratory of Advanced Photon Science and Technology, University of Science and Technology of China, Hefei, China

²Department of Physics and School of Emerging Technology, University of Science and Technology of China, Hefei 230026, China

³Anhui Key Laboratory of Condensed Matter Physics at Extreme Conditions, High Magnetic Field Laboratory, Chinese Academy of Sciences, Hefei 230031, China

⁴Department of Materials Science and Engineering, Southern University of Science and Technology, Shenzhen 518055, China

⁵International Center for Quantum Design of Functional Materials (ICQD), University of Science and Technology of China, Hefei, Anhui 230026, China

#These authors contributed equally to this work.

*Corresponding authors: (email:jiangcindy@ustc.edu.cn (Jiang J);
szhang2@ustc.edu.cn (Zhang SH); binxiang@ustc.edu.cn (Xiang B))

Note S1. Calculation of the valency and chemical stoichiometry from XPS data

We characterize the valence state for each composition in the ternary compound $\text{Ta}_2\text{Ni}_3\text{Te}_5$ by X-ray photoelectron spectroscopy (XPS). Clear characteristic signals subject to the three constituent elements can be readily identified in the total spectrum presented in Figure S1a. The zoomed-in plots near the peak positions of the three elements enable more detailed analyses on the involved orbitals. In Figure S1b, two dominant peaks of Ta exist at 23.0 and 25.0 eV, consistent with $4f_{7/2}$ of Ta^{2+} and $4f_{5/2}$ of Ta^{3+} , respectively [1,2]. In Figure S1c, the main peak at 852.9 eV is related to $2p_{3/2}$ of Ni^{2+} . Two adjacent peaks at 854.8 and 860.4 eV are resolved as the signal of $2p_{3/2}$ of Ni^{2+} , while other secondary peaks located at 870.2 and 873.8 eV are indexed to $2p_{1/2}$ of Ni and $2p_{1/2}$ of Ni^{2+} , respectively [3-5]. In Figure S1d, there are two dominant peaks of Te at 572.7 and 583.1 eV, which correspond to $3d_{5/2}$ of Te^{2-} and $3d_{3/2}$ of Te^{2-} , respectively [6,7]. Overall, even though multi-valency is resolved from the XPS measurements, the major peaks assign Ta^{2+} , Ni^{2+} and Te^{2-} as the prevailing species, chemically in line with the formula $\text{Ta}_2\text{Ni}_3\text{Te}_5$.

The stoichiometry of the synthesize $\text{Ta}_2\text{Ni}_3\text{Te}_5$ sample can be obtained from XPS spectra, with the percentage of element x (denoted as C_x) calculated by the formula [8,9]

$$C_x = \frac{\frac{I_x}{F_x}}{\frac{I_{\text{Ta}}}{F_{\text{Ta}}} + \frac{I_{\text{Ni}}}{F_{\text{Ni}}} + \frac{I_{\text{Te}}}{F_{\text{Te}}}}, \quad (1.1)$$

where I_{Ta} , I_{Ni} , and I_{Te} represent the peak area of Ta-4f, Ni-2p and Te-3d states respectively, and F represents atomic sensitivity factor of each element. The peak areas of Ta, Ni and Te in the XPS curves are calculated to be 134394.40, 428121.86

and 1126001.24 CPS.eV, with the sensitivity factors of 9.093, 20.765 and 42.333, respectively. Therefore, the calculated percentages of Ta, Ni and Te are 23.81%, 33.33% and 42.86%, respectively. The derived nominal chemical stoichiometry of $Ta_2Ni_{2.79}Te_{3.60}$ exhibits significant Tellurium-deficient characteristic, possibly due to partial oxidation of the sample as some minor signal for oxygen is also detected. Such imperfection, however, does not lay essential influence on the rich physics associated with in-plane anisotropy as revealed within the crystal.

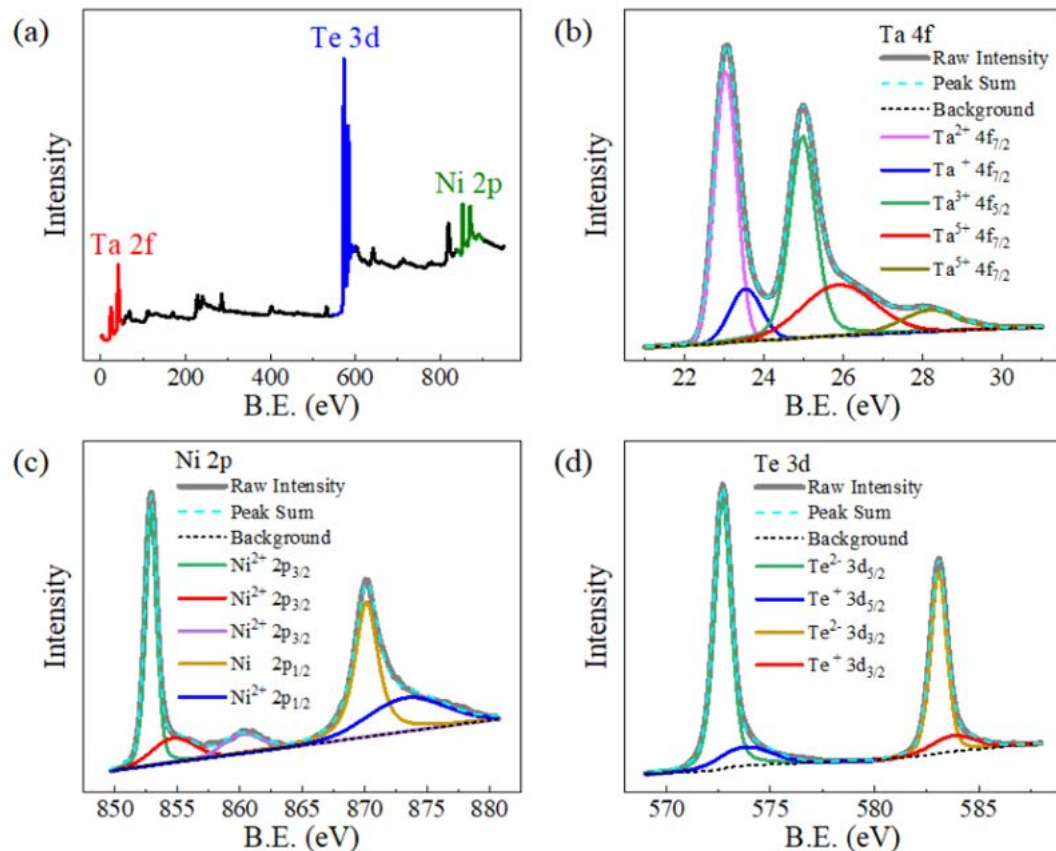


Figure S1. (a) X-ray photoelectron spectra of $Ta_2Ni_3Te_5$, and the zoomed-in plots near the peak positions of (b) Ta, (c) Ni and (d) Te.

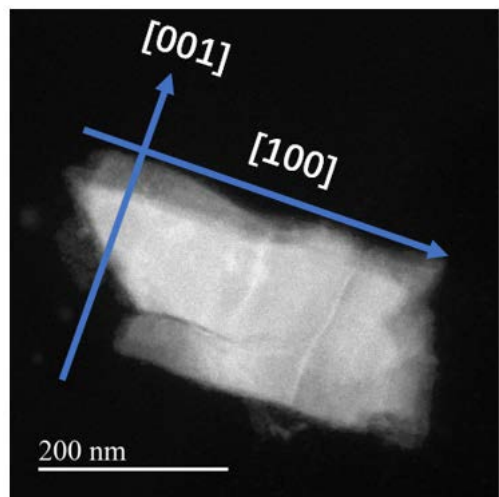


Figure S2. Low-magnification TEM image of the synthesized $\text{Ta}_2\text{Ni}_3\text{Te}_5$ sample.

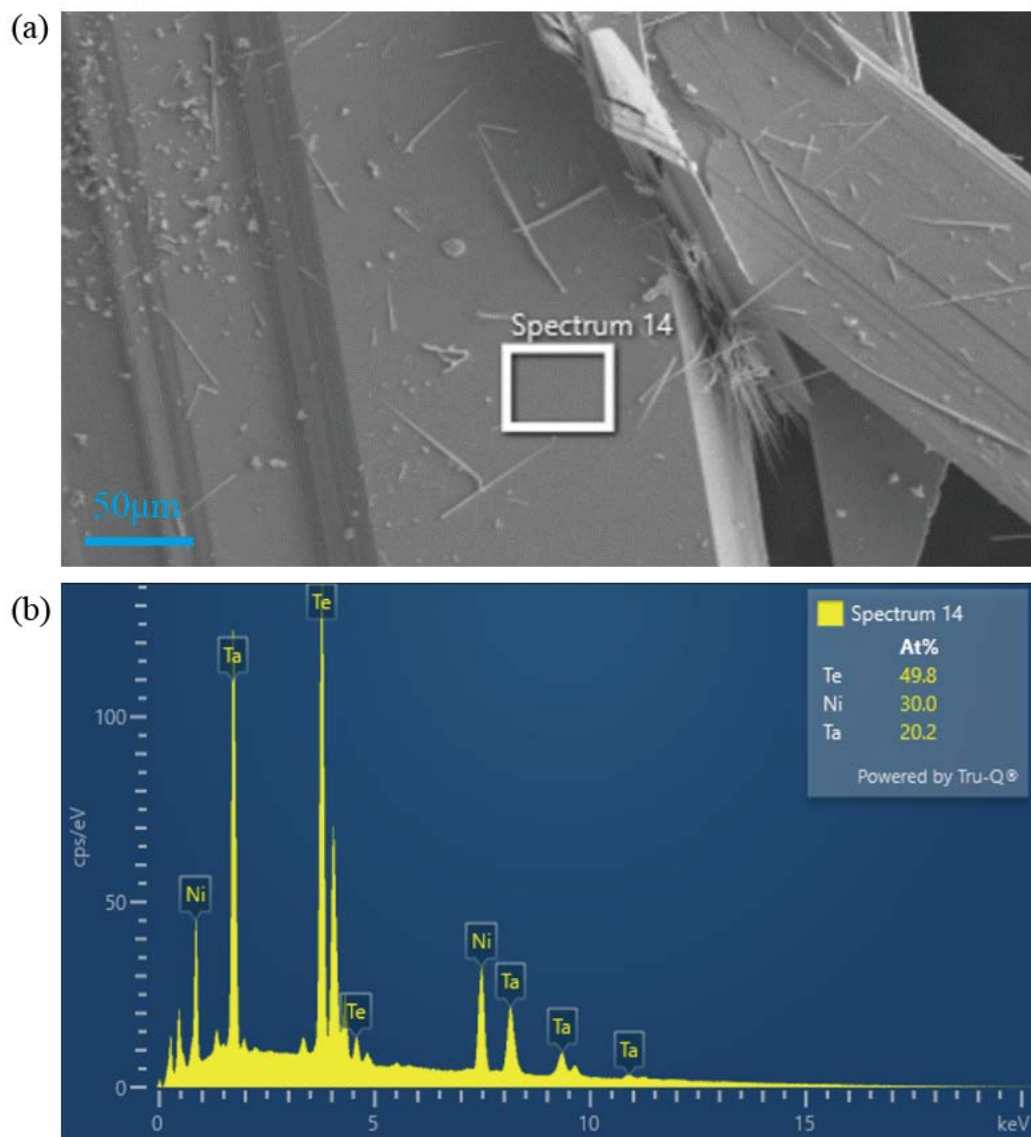


Figure S3. (a) Scanning electron microscopy (SEM) image of single crystal $\text{Ta}_2\text{Ni}_3\text{Te}_5$ (b) Energy dispersive X-ray spectroscopy spectra (EDS) measured within the area marked in (a) by the white rectangle.

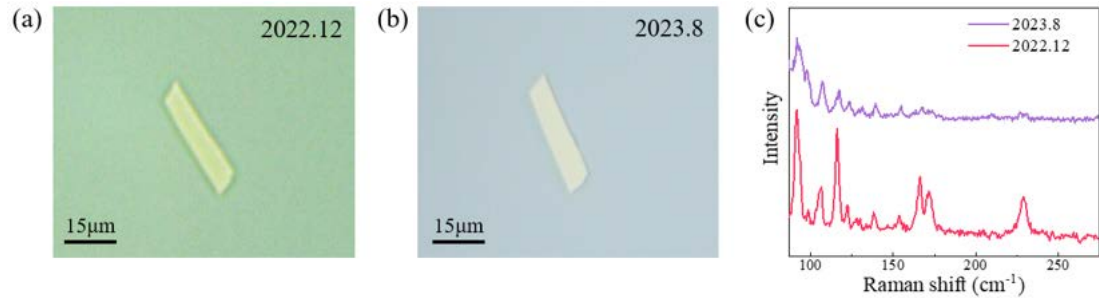


Figure S4. Optical images of a $\text{Ta}_2\text{Ni}_3\text{Te}_5$ sample taken (a) immediately after it was exfoliated and transferred onto the silicon oxide surface, and (b) after an 8-month exposure to air. (c) Raman spectra of this sample at different moments.

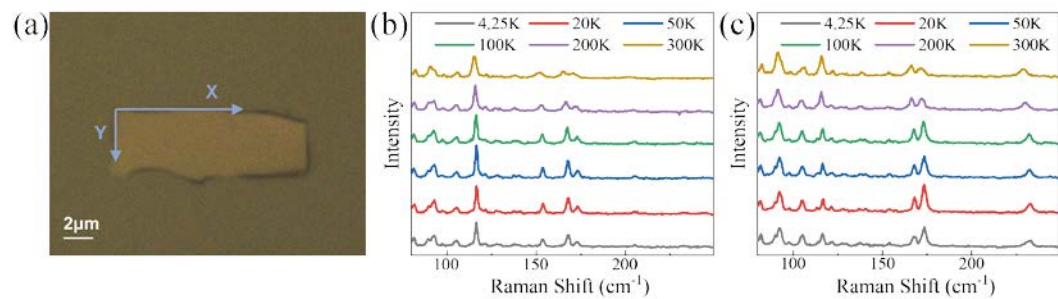


Figure S5. (a) Optical image of $\text{Ta}_2\text{Ni}_3\text{Te}_5$ sample for angle-dependent Raman measurement. (b-c) Raman spectra at different temperatures when laser is polarized to the (b) [001] and (c) [100] direction.

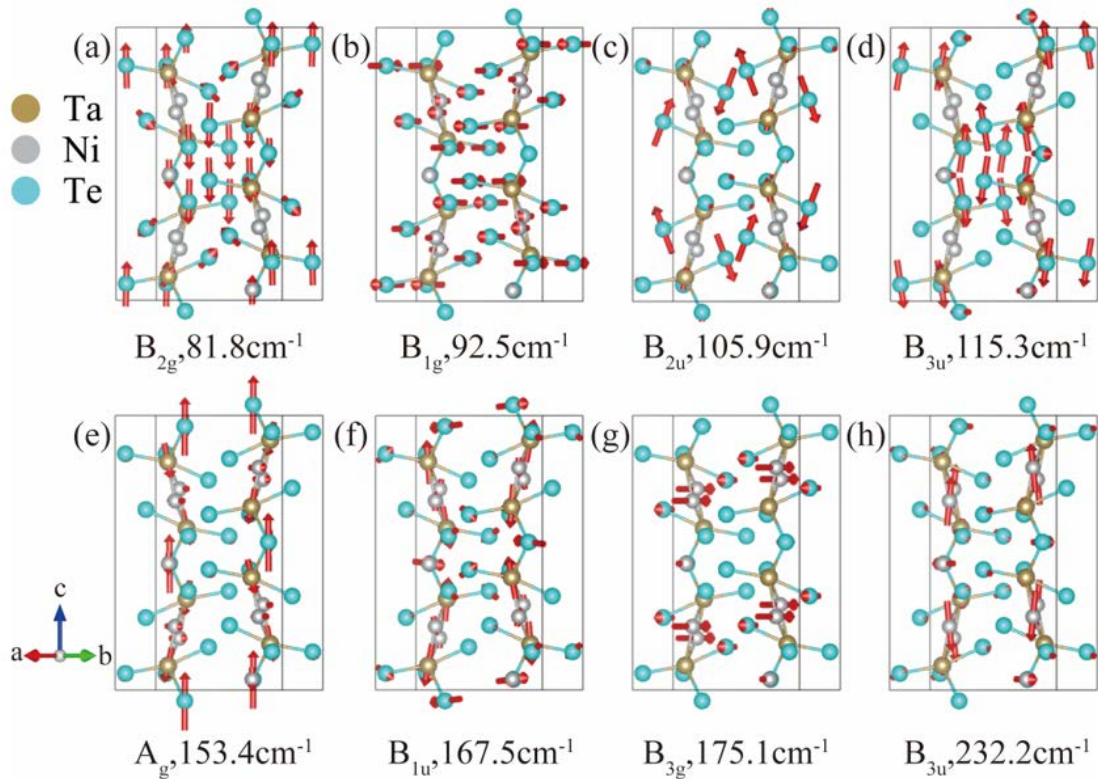


Figure S6. Calculated vibrational pattern of the Raman-active modes of $\text{Ta}_2\text{Ni}_3\text{Te}_5$, with mode symmetry and Raman shift denoted below each panel.

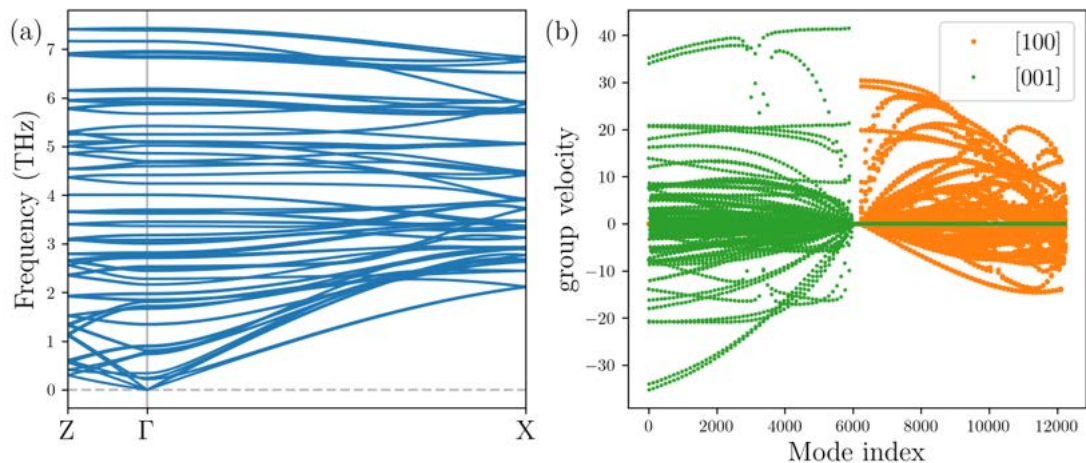


Figure S7. (a) Phonon dispersion and (b) group velocity distribution for vibrational modes on the high symmetry paths, corresponding to the [100] and [001] crystallographic axes in real space.

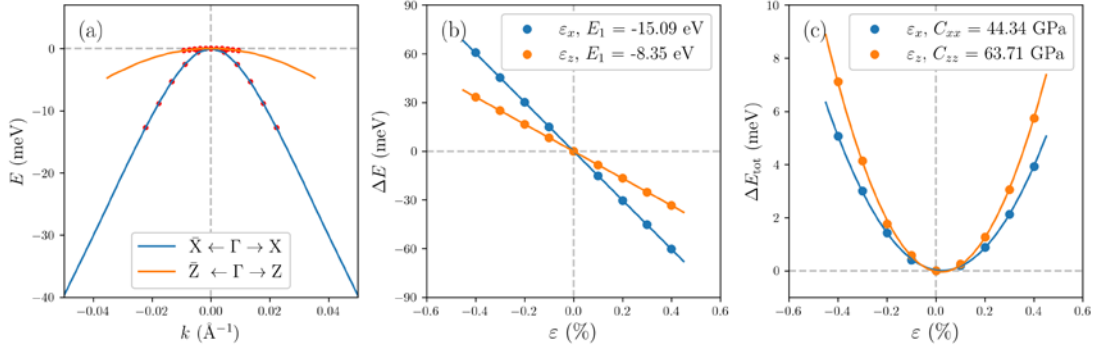


Figure S8. Calculation of hole carrier mobility based on the deformation potential theory. (a) The valence band dispersion near the Brillouin zone center. (b) The valence band maximum energy shift and (c) the strain energy, as functions of uniaxial strain along the [100] and [001] directions respectively. The dots are from DFT calculations while the curves are linear or parabolic fittings.

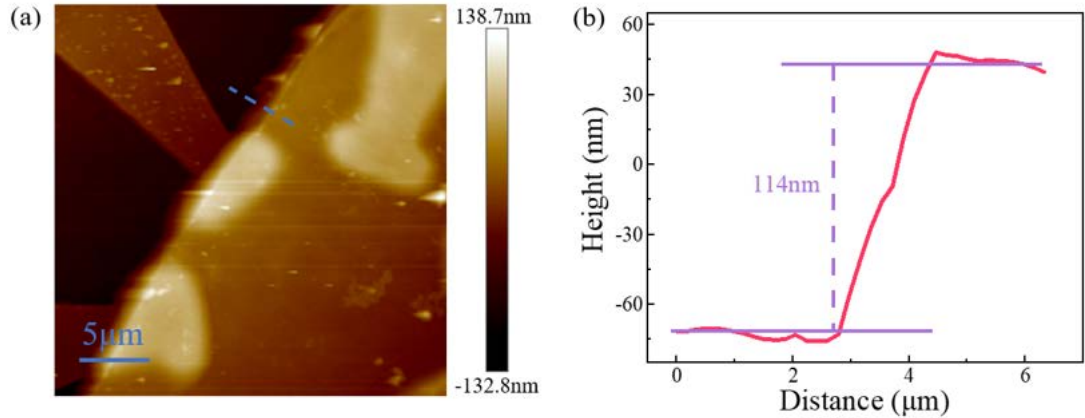


Figure S9. (a) Atomic force microscopy image of the device for electronic transport measurements. (b) The height profile corresponding to the dashed line cut near the sample edge in (a).

Table S1. The anisotropic ratios of conductance and mobility for some previously studied materials.

Material	Electronic property	anisotropic conductance ratio	anisotropic mobility ratio	ref.
WTe ₂	semimetal	270%	-	[10]
ZrTe ₅	semimetal	150%	207%	[11]
TaIrTe ₄	semimetal	200%	220%	[12]
Ta ₂ NiS ₅	semiconductor	178%	-	[13]
GeAs ₂	semiconductor	180%	190%	[14]
GeAs	semiconductor	3431%	460%	[15]
ReS ₂	semiconductor	750%	310%	[16]
TiS ₃	semiconductor	440%	760%	[17]
BP*	semiconductor	150%	180%	[18]
B-Arsenic	semiconductor	640%	2800%	[19]

* BP = Black phosphorus; B-Arsenic = Black Arsenic; “-”: data unavailable.

Supplementary References

- [1] Aminpirooz S, Becker L, Rossner H, *et al.* The structure of sodium intercalated 1T and 2H polytypes of TaS₂: a photoemission and SEXAFS study. *Surf Sci*, 1995, 331-333: 501-505
- [2] Khyzhun OY, Zhurakovskiy EA, Sinelnichenko AK, *et al.* Electronic structure of tantalum subcarbides studied by XPS, XES, and XAS methods. *Electron Spectrosc Relat Phenom*, 1996, 82: 179-192
- [3] Légaré P, Fritsch A. XPS Study of Transition Metal/Alumina Model Catalysts: Equilibrium and Energy Referencing. *Surf Interface Anal*, 1990, 15: 698-700

- [4] Venezia AM, Bertoncello R, Deganello G. X-Ray Photoelectron Spectroscopy Investigation of Pumice-supported Nickel Catalysts. *Surf Interface Anal*, 1995, 23: 239-247
- [5] Mansour AN. Copper Mg K_α XPS Spectra from the Physical Electronics Model 5400 Spectrometer. *Surf Sci Spectra*, 1994, 3: 202
- [6] Shalvoy RB, Fisher GB, Stiles PJ. Bond ionicity and structural stability of some average-valence-five materials studied by x-ray photoemission. *Phys Rev B*, 1977, 15: 1680-1697
- [7] Danaher WJ, Lyons LE, Marychurch M, *et al.* Chemical etching of crystal and thin film cadmium telluride. *Appl Surf Sci*, 1986, 27: 338-354
- [8] Li YG, Hasin P, Wu YY. Ni_xCo_{3-x}O₄ Nanowire Arrays for Electrocatalytic Oxygen Evolution. *Adv Mater*, 2010, 22: 1926
- [9] Fu Q, Yang L, Wang WH, *et al.* Synthesis and Enhanced Electrochemical Catalytic Performance of Monolayer WS_{2(1-x)}Se_{2x} with a Tunable Band Gap. *Adv Mater*, 2015, 27: 4732-4738
- [10] Choi YB, Xie Y, Chen CZ, *et al.* Evidence of higher-order topology in multilayer WTe₂ from Josephson coupling through anisotropic hinge states. *Nat Mater*, 2020, 19: 974-979
- [11] Seo SB, Nah S, Sajjad M, *et al.* Completely Anisotropic Ultrafast Optical Switching and Direction-Dependent Photocarrier Diffusion in Layered ZrTe₅. *Adv opt Mater*, 2023, 11: 2201544

- [12] Liu Y, Gu Q, Peng Y, *et al.* Raman Signatures of Broken Inversion Symmetry and In-Plane Anisotropy in Type-II Weyl Semimetal Candidate TaIrTe₄. *Adv Mater*, 2018, 30: 1706402
- [13] Li L, Gong P, Wang W, *et al.* Strong In-Plane Anisotropies of Optical and Electrical Response in Layered Dimetal Chalcogenide. *ACS Nano*, 2017, 11: 10264-10272
- [14] Li L, Gong P, Sheng D, *et al.* Highly In-Plane Anisotropic 2D GeAs₂ for Polarization Sensitive Photodetection. *Adv Mater*, 2018, 30: 1804541
- [15] Guo J, Liu Y, Ma Y, *et al.* Few-Layer GeAs Field-Effect Transistors and Infrared Photodetectors. *Adv Mater*, 2018, 30: e1705934
- [16] Wang YY, Zhou JD, Jiang J, *et al.* In-plane optical anisotropy in ReS₂ flakes determined by angle-resolved polarized optical contrast spectroscopy. *Nanoscale*, 2019, 11: 20199-20205
- [17] Island JO, Biele R, Barawi M, *et al.* Titanium trisulfide (TiS₃): a 2D semiconductor with quasi-1D optical and electronic properties. *Sci Rep*, 2016, 6: 22214
- [18] Liu H, Neal AT, Zhu Z, *et al.* Phosphorene: An Unexplored 2D Semiconductor with a High Hole Mobility. *ACS Nano*, 2014, 8: 4033-4041
- [19] Chen YB, Chen CY, Kealhofer R, *et al.* Black Arsenic: A Layered Semiconductor with Extreme In-Plane Anisotropy. *Adv Mater*, 2018, 30: 1800754